

Article

BAWSeg: A UAV Multispectral Benchmark for Barley Weed Segmentation

Haitian Wang¹ , Xinyu Wang¹ , Muhammad Ibrahim² , Dustin Severtson² , and Ajmal Mian^{1,*} 

¹ Department of Computer Science and Software Engineering, The University of Western Australia, 35 Stirling Highway, Crawley, WA 6009, Australia; haitian.wang@uwa.edu.au (H.W.); xinyu.wang@uwa.edu.au (X.W.); ajmal.mian@uwa.edu.au (A.M.)

² Department of Primary Industries and Regional Development (DPIRD), Government of Western Australia, 1 Nash St, Perth, WA 6000, Australia; muhammad.ibrahim@dpird.wa.gov.au (M.I.); dustin.severtson@dpird.wa.gov.au (D.S.)

* Correspondence: ajmal.mian@uwa.edu.au (A.M.)

Abstract

Accurate weed mapping in cereal fields requires pixel-level segmentation from UAV imagery that remains reliable across fields, seasons, and illumination. Existing multispectral pipelines often depend on thresholded vegetation indices, which are brittle under radiometric drift and mixed crop–weed pixels, or on single-stream CNN and Transformer backbones that ingest stacked bands and indices, where radiance cues and normalized index cues interfere and reduce sensitivity to small weed clusters embedded in crop canopies. We propose VISA (Vegetation-Index and Spectral Attention), a two-stream segmentation network that decouples these cues and fuses them at native resolution. The radiance stream learns from calibrated five-band reflectance using residual spectral-spatial attention to preserve fine textures and row boundaries that are attenuated by ratio indices. The index stream operates on vegetation-index maps with windowed self-attention to model local structure efficiently, state-space layers to propagate field-scale context without quadratic attention cost, and Slot Attention to form stable region descriptors that improve discrimination of sparse weeds under canopy mixing. To support supervised training and deployment-oriented evaluation, we introduce BAWSeg, a four-year UAV multispectral dataset collected over commercial barley paddocks in Western Australia, providing radiometrically calibrated blue, green, red, red edge, and near-infrared orthomosaics, derived vegetation indices, and dense crop, weed, and other labels with leakage-free block splits. On BAWSeg, VISA achieves 75.6% mIoU and 63.5% weed IoU with 22.8M parameters, outperforming a multispectral SegFormer-B1 baseline by 1.2 mIoU and 1.9 weed IoU. Under cross-plot and cross-year protocols, VISA maintains 71.2% and 69.2% mIoU, respectively. The BAWSeg data, VISA code, and trained models will be released upon publication.

Keywords: UAV; multispectral; weed mapping; barley; semantic segmentation; vegetation indices; radiometric calibration; orthomosaic; domain shift; benchmark dataset

1. Introduction

Barley is a major cereal crop cultivated across temperate and semi-arid regions worldwide, forming a core component of cereal-based farming systems alongside wheat and canola [1,2]. Across these systems, weeds remain the primary biotic constraint on yield, causing around 13% average global yield loss and billions of dollars of annual economic impact due to competition and herbicide resistance [3–6]. Herbicide-resistant populations of grass and broadleaf weeds are now common in many intensive cereal regions, motivating strong demand for spatially explicit weed management strategies.

arXiv:2603.01932v1 [cs.CV] 2 Mar 2026



Received:

Revised:

Accepted:

Published:

Copyright: © 2026 by the authors.

Licensee MDPI, Basel, Switzerland. This article is an open access article distributed under the terms and conditions of the [Creative Commons Attribution \(CC BY\) license](https://creativecommons.org/licenses/by/4.0/).

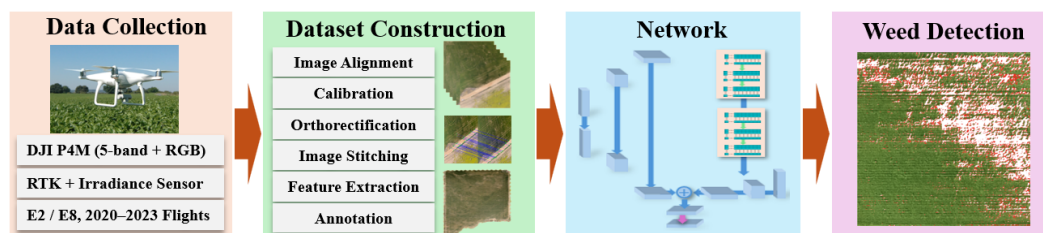


Figure 1. Overview of UAV multispectral data collection and BAWSeg dataset construction. The pipeline includes flight acquisition with RTK and irradiance sensors, radiometric calibration, orthorectification, stitching, feature extraction, annotation, and resulting crop–weed–soil maps.

In barley-based cropping systems, species such as annual ryegrass (*Lolium rigidum*) and wild radish (*Raphanus raphanistrum*) often dominate the weed spectrum, driving double-digit yield and quality losses when control is delayed or ineffective [7–10]. These pressures highlight the need for high-resolution sensing and mapping approaches capable of delineating weed patches at sub-field scales to support site-specific management [11,12].

Current practice in precision weed management combines manual scouting with proximal and remote sensing technologies, including satellite imagery, crewed aircraft surveys, and UAV-based multispectral imaging. These pipelines typically compute vegetation indices and apply threshold rules or shallow classifiers to distinguish crop, weed, and soil classes [11,13,14]. However, their reliance on hand-crafted indices, per-tile parameter tuning, and independent pixel or patch decisions limits robustness under variable illumination, canopy closure, and mixed crop–weed cover [15–17]. Deep convolutional and transformer-based encoder–decoder architectures improve spatial coherence but often rely on a single concatenated feature stream and are rarely evaluated under strong spatial or temporal domain shifts in cereal systems [18–21]. Despite rapid progress, publicly available benchmarks for weed segmentation do not yet match the practical deployment setting of cereal paddocks [22]. Many widely used weed datasets focus on image-level recognition or close-range field imagery, rather than field-scale UAV orthomosaics with pixel-level crop–weed masks. Large-scale aerial agriculture datasets (e.g., Agriculture-Vision) provide RGB–NIR patches with anomaly-style masks such as weed clusters, but they are not designed as calibrated multi-band UAV orthomosaics for explicit crop–weed semantic segmentation across multiple seasons and fields. As a consequence, prior work often reports results on single-field or single-season splits, making it difficult to quantify generalization under realistic spatial and temporal shifts.

To address these limitations, We propose VISA (Vegetation Index and Spectral Attention), a two-stream segmentation network that separates radiance-based and index-based reasoning. The radiance branch preserves fine row and patch boundaries through residual attention modules, while the index branch captures plot-level contextual patterns using attention and state-space mechanisms. Native-resolution features from both streams are fused to produce accurate crop–weed–background predictions, demonstrating improved segmentation performance under mixed canopy, variable illumination, and domain-shift conditions.

To enable supervised learning and deployment-oriented evaluation in cereal systems, we introduce BAWSeg, a four-year UAV multispectral benchmark collected over two commercial barley paddocks near Kondinin, Western Australia (2020–2023) using a DJI Phantom 4 Multispectral platform with RTK positioning and an upward irradiance sensor. Each campaign provides radiometrically calibrated five-band reflectance orthomosaics (blue, green, red, red edge, and near infrared), five derived vegetation indices (NDVI, GNDVI, EVI, SAVI, and MSAVI), and dense pixel annotations for crop, weed, and other classes that explicitly address crop–weed canopy mixing. Unlike existing resources that are either close-range field imagery or aerial datasets with anomaly-style labels, BAWSeg is designed as a reproducible UAV orthomosaic benchmark with consistent radiometry and leakage-free spatial block splits. These splits support three evaluation protocols—within-plot,

cross-plot, and cross-year (Fig. 1)—so that generalization across paddocks and seasons can be measured under realistic domain shifts rather than optimistic random sampling.

We evaluate our approach on representative barley paddocks in the Western Australian grainbelt, where herbicide-resistant weeds are prevalent. On within-plot test blocks, VISA achieves a mean Intersection over Union (mIoU) of 0.756 and a weed IoU of 0.635, with 22.8M parameters. Compared with a SegFormer-B1 baseline trained under identical conditions, mIoU increases by about 2% and weed IoU by 3% at similar throughput. Under cross-plot and cross-year evaluations, mean IoUs of 0.71 and 0.69 are maintained, demonstrating robustness under spatial and temporal domain shifts.

Our main contributions are summarized as follows:

- **VISA** model: a two-stream network that integrates radiance and vegetation index reasoning for improved segmentation under mixed canopy scenarios.
- **BAWSeg** benchmark: a UAV multispectral dataset for barley fields with high-resolution, pixel-level crop, weed, and soil annotations under realistic field and seasonal variations.
- Evaluation protocol: systematic within-plot, cross-plot, and cross-year benchmarks that demonstrate the utility of BAWSeg for model assessment and precision weed mapping research.

2. Related Work

We group prior work into three areas: UAV multispectral weed mapping with index based pipelines, crop–weed semantic segmentation using convolutional encoder–decoder networks on RGB or multispectral inputs, and Transformer or state space models for remote sensing segmentation. These studies provide the baselines and context for our two stream radiance–index model.

UAV multispectral imagery is widely used for site specific weed management and crop–weed discrimination, typically by deriving vegetation indices such as NDVI, GNDVI, SAVI and MSAVI from calibrated red, green, red edge and near infrared bands and then classifying crop, weed and soil with threshold rules or shallow models including support vector machines, random forests and multilayer perceptrons [13,14,23–25]. Object based image analysis combined with random forests has been used to segment homogeneous regions and generate prescription maps in maize and sunflower, while exploiting only local spectral and texture descriptors [26–28]. Semi supervised systems and feature selection schemes further improve robustness under limited labels by stacking multiple vegetation indices into per pixel or small patch feature vectors for weed mapping in heterogeneous fields [15,29,30]. More recent work integrates multispectral UAV data with ancillary information and ensemble learners to estimate weed density at plot scale in cereal crops [16,31,32]. Across these studies, decisions are usually taken independently for each pixel or patch using hand designed spectral indices and hard labels that assign a single class per pixel, which restricts the use of row level and field level structure and does not explicitly model the uncertainty of mixed pixels where crop plants and weeds occupy the same footprint.

UAV crop–weed mapping has increasingly been formulated as semantic segmentation with convolutional or encoder–decoder backbones such as U-Net, SegNet and DeepLabv3+, adapted from generic vision to field imagery [18–20]. Early agricultural deployments trained fully convolutional networks on UAV or ground imagery to delineate crop rows and weed patches but largely followed single-stream designs [21,33,34]. Most studies use RGB or multispectral bands and append a small set of vegetation indices as extra channels, then feed the concatenated tensor into one encoder that must learn spectral contrast and geometric texture without explicit separation of radiance and normalized index cues [21,33,35]. Architectures that dedicate an index-aware branch or explicitly decouple spectral ratio information from spatial structure remain uncommon in the UAV literature, as summarized by recent reviews of deep learning for weed detection and drone imaging in agriculture [17,36]. Supervision typically relies on hard one-hot pixel labels, so mixed pixels where crop and weed co-occur are forced to a single class and label uncertainty is rarely modeled [17,34]. These choices limit robustness under illumination change and can reduce sensitivity to small weed clusters embedded in crop canopies in orthomosaics [33,35,37].

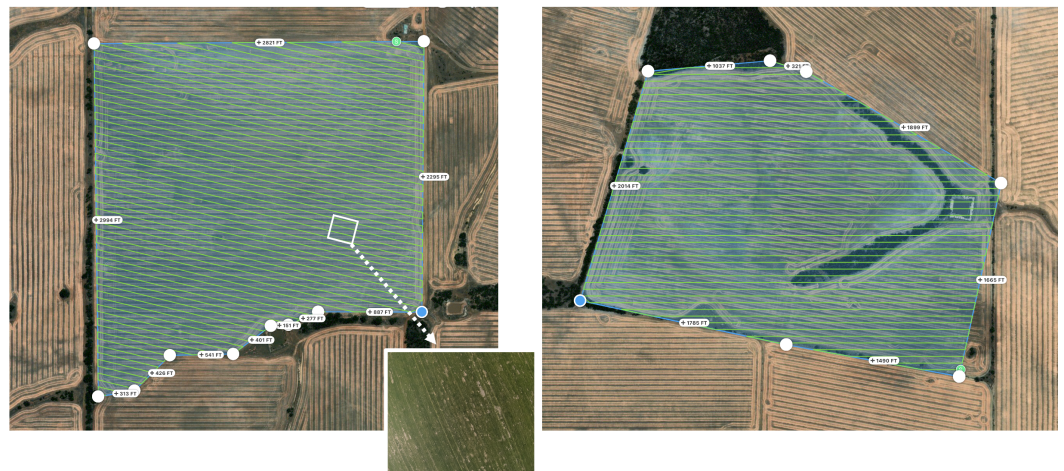


Figure 2. Planned flight paths for the Kondinin experimental fields. Left, E8 polygon and survey lines planned in GSPPro. Right, E2 polygon with the same overlap and altitude parameters. The inset shows a representative interior tile used for quality control of row orientation and texture.

Transformer architectures have been adopted for remote sensing segmentation to capture long range dependencies that are difficult for convolutional encoders. Early work adapts the Vision Transformer and Swin Transformer to aerial and satellite imagery using self attention on patch tokens or shifted windows [38,39], followed by hybrids such as SegFormer and related CNN Transformer models with lightweight decoders for high resolution land cover from RGB or multispectral inputs [40,41]. Subsequent methods specialize transformers for remote sensing through tailored tokenization and encoder–decoder designs, including RSTFormer and UNetFormer for urban scenes and river networks and SpectralFormer for hyperspectral land cover classification [42–44]. In agriculture, transformer variants are mainly used for crop type mapping and field level weed detection from UAV or satellite imagery with single stream ViT style backbones on reflectance stacks or RGB composites and hard pixel labels [45,46]. Recent visual state space models such as VMamba and RS3Mamba extend selective state space layers to semantic segmentation and achieve competitive performance on benchmarks such as LoveDA and ISPRS Vaihingen [47,48], yet most transformer and Mamba based approaches still employ a single feature stream without explicit vegetation index reasoning, structured grouping modules such as Slot Attention or annotation protocols that represent mixed crop–weed canopies and soft label uncertainty.

3. Materials and Methods

This section specifies the complete workflow used to build the BAWSeg benchmark and to develop the VISA segmentation model. It first describes the UAV acquisition setup, radiometric calibration and preprocessing steps that produce georeferenced multispectral orthomosaics, followed by the annotation procedure, patch extraction, and leakage-free block splits that support within-plot, cross-plot, and cross-year evaluation. It then details the two-stream architecture, feature fusion, training objective, and implementation settings used consistently across all experiments.

3.1. Dataset Construction

We first give details of the BAWSeg dataset since the segmentation model is designed to exploit the information available in this dataset. BAWSeg is a multispectral dataset collected by a UAV from repeated field campaigns. It covers platform and radiometric calibration, mission geometry for uniform coverage, and preprocessing that rectifies, coregisters, orthorectifies, and mosaics all bands. It then outlines patch extraction, leakage-free splits, augmentation, and a dense polygon-based pixel annotation protocol with quality control. The process preserves traceability and consistent radiometry and geometry for reliable training and evaluation.

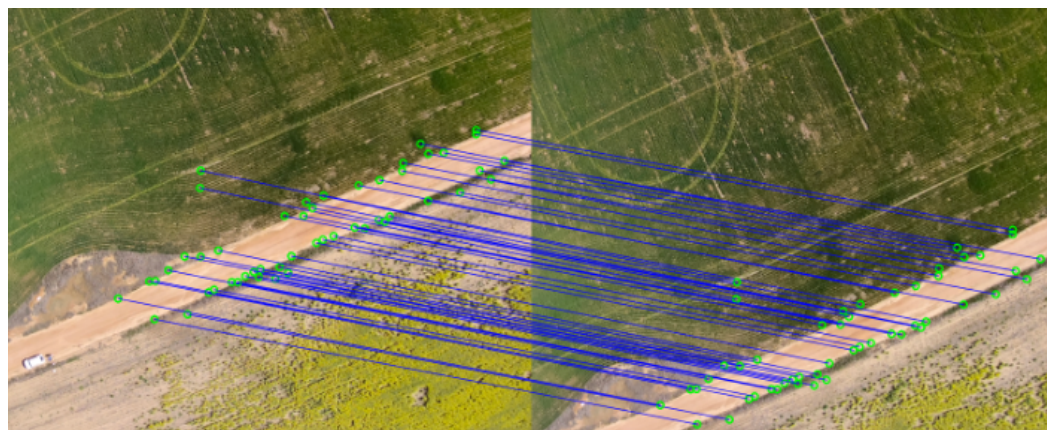


Figure 3. Example of keypoint inliers for cross band and inter frame alignment. Green circles denote SIFT keypoints and blue lines denote matches retained after RANSAC.

3.1.1. Acquisition Platform and Configuration

Image capture used a DJI Phantom 4 Multispectral (P4M) RPAS with six synchronized cameras, five narrowband monochrome sensors (blue, green, red, red edge and NIR) and one RGB sensor. An upward irradiance sensor logged downwelling light for every exposure and an RTK module with TimeSync referenced geotags to the camera center. The gimbal was fixed at nadir (-90°). Exposure control operated in manual mode with fixed white balance and ISO for each mission and shutter speed was set to avoid motion blur at the commanded groundspeed. Radiometric reference data were collected with a calibrated Lambertian reflectance panel using nadir frames acquired before and after each mission and whenever the solar zenith changed noticeably during flight, with the irradiance sensor enabled for all captures. Simple capture quality gates monitored shutter speed, saturation, irradiance validity and gimbal status and any pass that violated these checks was repeated at the same altitude and speed. During acquisition, EXIF metadata recorded exposure parameters, RTK position, ellipsoidal height, gimbal yaw, pitch and roll, and irradiance flags. After each mission these fields were parsed into a CSV file with frame identifiers, timestamps, platform pose and quality indicators. All data were stored in a mission specific directory hierarchy indexed by date and site with separate locations for raw multispectral and RGB frames, metadata tables and integrity checksums, which preserves capture conditions for the radiometric normalization and orthomosaic generation described in the next subsection.

3.1.2. Flight Mission Geometry and Coverage

Two experimental barley fields near Kondinin, Western Australia, were surveyed in four UAV campaigns from 2020 to 2023. The mapped polygons, centred at E2 (lat -32.508363 , lon 118.338139) and E8 (lat -32.516563 , lon 118.353799), cover 0.6046 km^2 in total. Missions were planned in DJI Ground Station Pro using lawnmower patterns within each polygon, with the camera fixed at nadir, flight altitude set to 120 m above ground level, and both forward and side overlap set to 80%. Line spacing, trigger intervals and groundspeed were derived from these parameters and applied uniformly during acquisition. Takeoff and landing points were placed on access tracks outside the cropped area and flights were scheduled between 10:30 and 14:30 local time, with segments repeated if wind or illumination changed noticeably to keep conditions consistent within each field. For every sortie, the mission plan and realised trajectory were logged with the field identifier, including polygon vertices, line spacing and commanded speed. Figure 2 illustrates the resulting coverage pattern, where survey lines follow the field boundaries and provide stable overlap for subsequent orthomosaic generation and feature matching across the four campaigns.

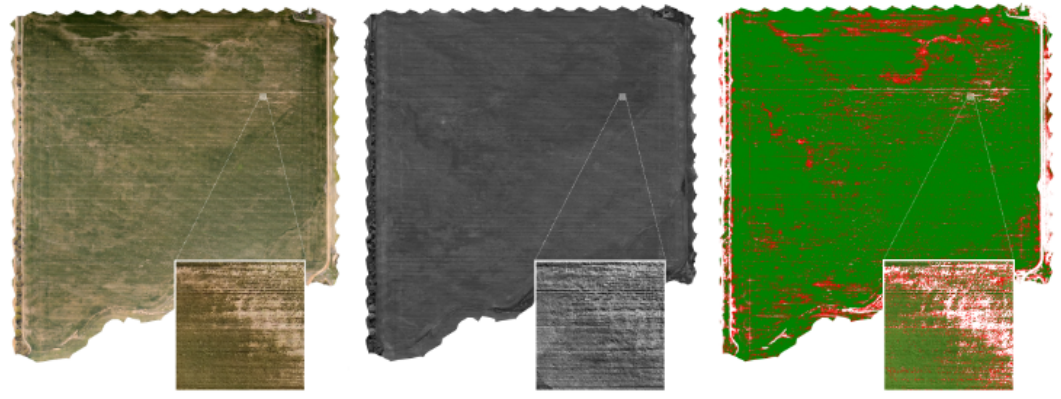


Figure 4. From left to right, RGB orthomosaic, a single-band reflectance map, and the hard label map. Green denotes crop, red denotes weed, and white denotes other.

3.1.3. Image Preprocessing

Raw multispectral frames are converted to single precision arrays, filtered by capture quality flags, and denoised with a 3×3 median kernel applied independently to the R, G, B, NIR and RedEdge bands. Frames that contain more than 0.5% saturated pixels in any band are discarded, and lens vignetting and distortion are corrected using the vendor calibration so that all subsequent steps operate on rectified images. Cross band alignment then registers every band to the green reference. SIFT keypoints are extracted per band, descriptor matches are filtered with a Lowe ratio test and RANSAC, and a projective homography is estimated for each band, which is adequate for the near planar scenes at 120 m altitude. The transform is refined by maximizing the enhanced correlation coefficient on a grid of small windows and registration quality is reported as the median reprojection error, with frames above a 0.5 pixel threshold flagged for reprocessing. Figure 3 illustrates typical inlier correspondences after matching and RANSAC.

Panel based radiometric calibration converts the registered digital numbers to per band reflectance that is consistent across sorties. For each band a scale factor is derived from pre and post flight panel captures and the upward irradiance sensor, and per frame reflectance is adjusted for exposure and irradiance variation, clipped to a fixed range, and stored as float32. Orthorectification then uses RTK geotags and structure from motion in Agisoft Metashape to estimate camera poses and a digital elevation model. All bands of each frame are treated as a rigid group and are projected onto the elevation model into a common ground coordinate system. Seamline optimization and blending within the overlap generate multispectral and RGB orthomosaics without exposure compensation for the analytical bands so that radiometric consistency is preserved. The final per band mosaics are exported as tiled GeoTIFFs for index computation and patch extraction in the dataset pipeline.

3.1.4. Annotation and Dataset Finalization

Pixels in the multispectral orthomosaics are labelled at native resolution as barley crop, ryegrass weed or other, where other covers soil, wheel tracks and infrastructure. Orthorectified and radiometrically normalized mosaics are tiled, and a vegetation mask derived from NDVI restricts annotation to canopy pixels while nonvegetation and invalid pixels are assigned other or an ignore value. Within this mask annotators use a GIS editor with orthomosaic, NDVI and RGB composites to draw crop and weed polygons, and very small polygons are discarded. The polygons are rasterised by assigning each pixel the class of the polygon that contains its centre, overlaps are resolved in favour of weed polygons so that mixed canopies follow the weed label, and remaining vegetation pixels outside all polygons are kept as other. Each tile is annotated by one operator and checked by a second, and a stratified subset is reannotated to maintain consistent class usage across fields and years. The final labels are stored as single channel GeoTIFFs with other equal to zero, crop equal to one, weed equal to two and ignore equal to two hundred and fifty five, and during training this map

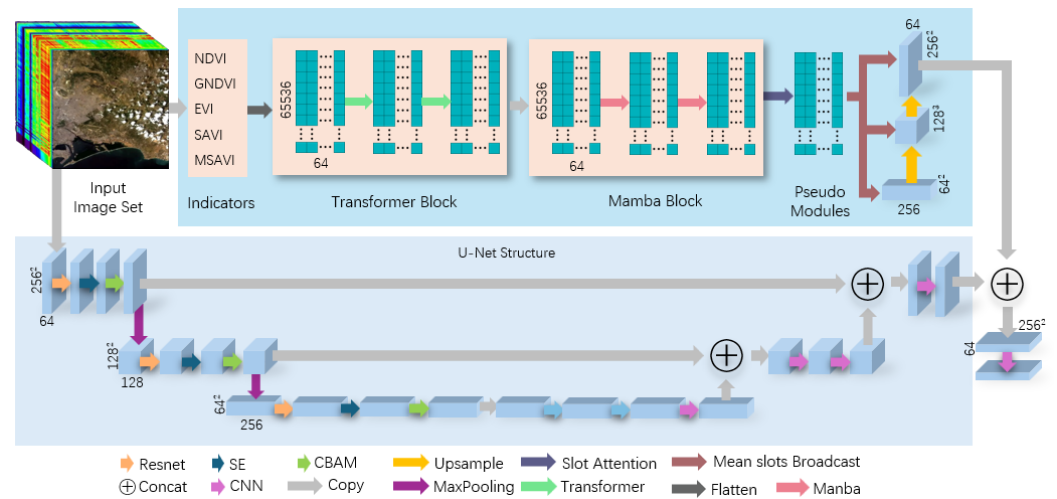


Figure 5. Overview of the proposed pipeline. Bottom: SRAB radiance stream with residual attention and a U-Net decoder. Top: vegetation-index stream with windowed self-attention, Mamba blocks, Slot Attention with mean-slot broadcast, and a scale-aligned decoder. Right: fusion head that concatenates the two 64-channel feature maps at the native resolution to generate class logits.

is converted to one hot targets $y_{b,c,h,w} \in \{0, 1\}$ with the ignore value forming a binary mask that removes those pixels from the supervised loss.

3.2. Methods

We propose VISA, a two-stream segmentation architecture that leverages complementary cues from vegetation indices and multispectral imagery. The model aims to jointly capture fine spatial detail and field-scale agronomic patterns that are difficult to resolve from a single feature stream. As shown in Figure 5, the network contains two parallel branches, a *Vegetation-Index Branch* that operates on normalized vegetation indices and a *Spectral Residual Attention Branch (SRAB)* that processes the multispectral radiance cube. Both branches output 64-channel feature maps at native 256×256 resolution, which are fused by a shallow head to produce per-pixel logits for crop, weed, and background classes. This design separates low-level radiometric reasoning from high-level vegetation context modeling, improving robustness under illumination changes and canopy mixing. Let B denote batch size. Each training sample is a 256×256 patch cropped from a georeferenced orthomosaic. The radiance input is a five-band reflectance tensor $X^{\text{raw}} \in \mathbb{R}^{B \times 5 \times H \times W}$ with $H=W=256$, ordered as (B, G, R, RE, NIR) after band co-registration. The index input is a five-channel tensor $X^{\text{id}} \in \mathbb{R}^{B \times 5 \times H \times W}$ formed by vegetation index maps computed from the same reflectance bands. Unless otherwise stated, convolutions use zero padding and preserve spatial size. Both branches output native-resolution features in $\mathbb{R}^{B \times 64 \times 256 \times 256}$ and are fused to predict $C=3$ semantic classes $\{\text{other, crop, weed}\}$, while the ignore label is excluded from supervision by a binary mask. The configuration used throughout the paper fixes the embedding width at $d=64$, the window size at $s=8$ for windowed self-attention, the number of Slot Attention groups at $K=6$, and the number of Slot Attention refinement iterations at $T=3$.

3.2.1. Vegetation-Index Modeling Branch

To complement raw-band learning with normalized spectral reasoning, we introduce a *vegetation-index modeling branch* that operates on a compact stack of five indices $\{\text{NDVI, GNDVI, EVI, SAVI, MSAVI}\}$ derived from calibrated reflectance. These indices emphasize vegetation vigor and suppress illumination variability, allowing the model to capture agronomic patterns that arise from cross-band interactions rather than single-band responses. Indices are computed from calibrated reflectance with a small stabilizer $\epsilon=10^{-6}$. For example, $\text{NDVI} = (\text{NIR} - R) / (\text{NIR} + R + \epsilon)$, $\text{GNDVI} = (\text{NIR} - G) / (\text{NIR} + G + \epsilon)$, and $\text{SAVI} = 1.5(\text{NIR} - R) / (\text{NIR} + R + 0.5 + \epsilon)$. We

apply a fixed per-index standardization using statistics computed on the training split only. For the i th index channel, $\tilde{X}_i^{\text{idx}} = (X_i^{\text{idx}} - \mu_i) / (\sigma_i + \epsilon)$, and the same (μ_i, σ_i) are reused for validation and test data to avoid leakage.

Each index map is linearly standardized and projected to an embedding width $d=64$ via a 1×1 convolution and LayerNorm:

$$Z = \text{LN}(W^{\text{proj}} \tilde{X}^{\text{idx}} + b^{\text{proj}}), \quad Z \in \mathbb{R}^{B \times d \times 256 \times 256}. \quad (1)$$

Here $W^{\text{proj}} \in \mathbb{R}^{d \times 5 \times 1 \times 1}$ and $b^{\text{proj}} \in \mathbb{R}^d$ implement a 1×1 projection from five indices to $d=64$ channels. $\text{LN}(\cdot)$ denotes LayerNorm applied over the channel dimension at each spatial location, which stabilizes training under index magnitude variations across seasons and fields.

We reshape Z into non-overlapping 8×8 windows and apply two lightweight Transformer encoder layers with windowed self-attention. This design preserves local spatial coherence (e.g., crop rows and patch textures) while avoiding the quadratic complexity of global attention. A decomposed relative positional bias further enhances geometric sensitivity within each window.

Concretely, Z is partitioned into $N_w = (H/s)(W/s)$ non-overlapping windows. For each window, we flatten its $s \times s$ grid into a token matrix $U \in \mathbb{R}^{n \times d}$ with $n = s^2$. Multi-head attention uses h heads with per-head width $d_h = d/h$. For head j , queries, keys, and values are $Q_j = UW_j^Q$, $K_j = UW_j^K$, and $V_j = UW_j^V$, where $W_j^Q, W_j^K, W_j^V \in \mathbb{R}^{d \times d_h}$. The attention output is computed as

$$\text{Attn}_j(U) = \text{Softmax}\left(\frac{Q_j K_j^T}{\sqrt{d_h}} + B_j^{\text{rel}}\right) V_j, \quad (2)$$

where $B_j^{\text{rel}} \in \mathbb{R}^{n \times n}$ is a learnable relative positional bias indexed by 2D offsets within the window. The h head outputs are concatenated and projected back to width d by $W^O \in \mathbb{R}^{d \times d}$.

Each encoder layer follows a pre-norm residual form

$$\hat{U} = U + \text{WSA}(\text{LN}(U)), \quad U^+ = \hat{U} + \text{FFN}(\text{LN}(\hat{U})), \quad (3)$$

where WSA denotes the multi-head windowed attention above. FFN is a position-wise two-layer perceptron with GELU nonlinearity applied independently to each token. In our configuration, $s=8$ and $h=8$, which keeps attention local to 64 tokens per window while preserving row-level texture cues.

To capture field-wide regularities, we append two Mamba-style state-space blocks that act as gated 1D filters along the token sequence. For token embedding u_t , the selective update follows:

$$x_{t+1} = \bar{A} \odot x_t + \bar{B} \odot (u_t \odot \sigma(W_g u_t)) \quad (4)$$

We apply the state-space blocks on a 1D token sequence obtained by raster scanning the $H \times W$ grid, giving $L=HW$ tokens. At step t , $u_t \in \mathbb{R}^d$ is the token embedding and $x_t \in \mathbb{R}^d$ is the state vector. $\bar{A} \in \mathbb{R}^d$ and $\bar{B} \in \mathbb{R}^d$ are learned per-channel coefficients after discretization, and \odot denotes element-wise multiplication. The gate $\sigma(W_g u_t)$ uses $W_g \in \mathbb{R}^{d \times d}$ and modulates input injection to suppress ambiguous mixed pixels. This recurrence updates each token in linear time in L and does not incur the quadratic cost of global attention, which is important for field-scale context modeling on dense orthomosaics.

Finally, we apply Slot Attention ($K=6$ slots, $T=3$ iterations) to group tokens into structured semantic regions (e.g., crop canopy, weed clusters, soil). The aggregated descriptor is broadcasted back to the spatial grid, forming a feature map $F^{\text{idx}} \in \mathbb{R}^{B \times 64 \times 256 \times 256}$ that carries globally consistent vegetation cues. Let $U^+ \in \mathbb{R}^{L \times d}$ denote the token matrix after windowed attention and state-space

filtering. Slot Attention maintains K slot vectors $S = \{s_k\}_{k=1}^K$ with $s_k \in \mathbb{R}^d$. At each refinement iteration, we compute attention weights between tokens and slots by

$$a_{t,k} = \frac{\exp(\langle W^q s_k, W^k u_t \rangle / \sqrt{d})}{\sum_{k'=1}^K \exp(\langle W^q s_{k'}, W^k u_t \rangle / \sqrt{d})}, \quad (5)$$

where u_t is the t th token, $W^q, W^k \in \mathbb{R}^{d \times d}$, and $\langle \cdot, \cdot \rangle$ is the dot product. Slot updates aggregate values $v_t = W^v u_t$ with $W^v \in \mathbb{R}^{d \times d}$,

$$\Delta s_k = \sum_{t=1}^L a_{t,k} v_t, \quad s_k \leftarrow \text{GRU}(s_k, \Delta s_k) + \text{MLP}(\text{LN}(s_k)), \quad (6)$$

where the GRU and MLP are shared across slots. After T iterations, we compute the mean-slot descriptor $m = \frac{1}{K} \sum_{k=1}^K s_k$ and broadcast it to all spatial locations by $U_t^b = U_t^+ + W^b m$ with $W^b \in \mathbb{R}^{d \times d}$. This mean-slot broadcast injects a global grouping prior while retaining token-level variation for small weed clusters. Finally, U^b is reshaped back to $\mathbb{R}^{B \times d \times H \times W}$ and mapped to $F^{\text{id}x}$ by a 3×3 convolution followed by normalization.

This feature map is decoded by shallow convolutional upsampling layers and supervised by an auxiliary segmentation loss weighted by 0.3, encouraging early-stage discriminative learning in the index domain.

3.2.2. Spectral Residual Attention Branch

In parallel, the *spectral residual attention branch* learns directly from calibrated multispectral reflectance $\{B, G, R, \text{RE}, \text{NIR}\}$ to retain subtle spectral contrasts that ratio-based indices may suppress. The branch adopts a three-stage residual-attention encoder followed by a symmetric decoder.

Each stage stacks two *residual-attention units* consisting of convolutional bodies, squeeze-excitation channel weighting, and CBAM-style spatial gating. Formally, a unit transforms feature U as

$$Y = \text{CBAM}(\text{SE}(U + W_2 * \text{GELU}(W_1 * U))) \quad (7)$$

In this unit, W_1 and W_2 are 3×3 convolutions that preserve spatial size. The residual branch $U + W_2 * \text{GELU}(W_1 * U)$ increases nonlinearity while keeping gradient flow stable.

The squeeze-excitation operator produces channel weights from global statistics. Let $g = \frac{1}{HW} \sum_{h,w} U_{c,h,w} \in \mathbb{R}^C$ be global average pooled features for C channels. SE computes $a = \sigma(W_2^{\text{se}} \text{GELU}(W_1^{\text{se}} g))$ and rescales channels by $U_{c,h,w}^{\text{se}} = a_c U_{c,h,w}$, where W_1^{se} and W_2^{se} are learned linear layers and $\sigma(\cdot)$ is the sigmoid.

CBAM further applies spatial gating conditioned on local context. Given U^{se} , we form a spatial descriptor by concatenating average-pooled and max-pooled maps across channels and apply a 7×7 convolution to obtain a spatial mask $M^{\text{sp}} \in [0, 1]^{H \times W}$. The output is $Y_{c,h,w} = M_{h,w}^{\text{sp}} U_{c,h,w}^{\text{se}}$, which suppresses background clutter and enhances thin weed structures aligned with crop rows.

Encoded features with widths $\{64, 128, 256\}$ are hierarchically aggregated by transposed convolutions and refinement blocks, restoring native 256×256 resolution. The resulting feature map $F^{\text{raw}} \in \mathbb{R}^{B \times 64 \times 256 \times 256}$ encodes high-frequency appearance cues complementary to the vegetation-index pathway.

The encoder uses three resolution levels with channel widths $\{64, 128, 256\}$. Spatial resolution is reduced by a factor of two between levels, and the decoder restores 256×256 resolution with learnable upsampling. Skip connections from the three encoder levels are concatenated into the corresponding decoder stages to preserve row boundaries and small weed fragments that are lost under repeated downsampling. The last decoder stage outputs F^{raw} at width 64 to match the index branch for fusion.

Together, these two streams—one semantic and index-driven, the other spectral and residual-attentive—form a dual-branch encoder that captures both normalized vegetation signals and raw spectral variations for robust UAV weed segmentation.

3.2.3. Feature Fusion and Prediction Head

After decoding, the two streams provide aligned native-resolution feature maps with complementary content: the radiance stream preserves high-frequency textures and spectral contrast, whereas the index stream injects global semantic priors shaped by attention and state-space filtering. The fusion head performs local channel mixing and produces per-pixel logits for the target classes.

Both feature maps are aligned on the same 256×256 grid and share the same channel width, which allows fusion without interpolation. The classifier predicts $C=3$ logits per pixel and the ignore label is implemented only in the supervision mask rather than as a prediction class.

Let $Y^{\text{raw}}, Y^{\text{idX}} \in \mathbb{R}^{B \times 64 \times 256 \times 256}$ be the branch outputs at native resolution. They are concatenated along the channel axis to form $F^{\text{cat}} = \text{Concat}(Y^{\text{raw}}, Y^{\text{idX}}) \in \mathbb{R}^{B \times 128 \times 256 \times 256}$. The fusion block first performs channel mixing and local aggregation by a 3×3 convolution with zero padding, followed by batch normalization and a rectified linear activation. Denote the fusion kernel $W^{\text{fus}} \in \mathbb{R}^{64 \times 128 \times 3 \times 3}$ and bias $b^{\text{fus}} \in \mathbb{R}^{64}$. The pre-activation fused map $F \in \mathbb{R}^{B \times 64 \times 256 \times 256}$ is defined component wise as

$$F_{b,q,h,w} = (W^{\text{fus}} * F^{\text{cat}})_{b,q,h,w} + b_q^{\text{fus}}, \quad 1 \leq q \leq 64. \quad (8)$$

Batch normalization with learned affine parameters γ_q, β_q and an ε -stabilized variance is then applied per output channel, followed by a rectified activation. Writing μ_q and σ_q^2 for the batch-wise moments of $F_{b,q,\cdot,\cdot}$,

$$F'_{b,q,h,w} = \max \left\{ 0, \gamma_q \frac{F_{b,q,h,w} - \mu_q}{\sqrt{\sigma_q^2 + \varepsilon}} + \beta_q \right\}. \quad (9)$$

The prediction head maps F' to C semantic classes by a 1×1 convolution $W^{\text{cls}} \in \mathbb{R}^{C \times 64 \times 1 \times 1}$ with bias $b^{\text{cls}} \in \mathbb{R}^C$ to produce the per-pixel logits $Z \in \mathbb{R}^{B \times C \times 256 \times 256}$.

$$Z_{b,c,h,w} = \sum_{q=1}^{64} W_{c,q,1,1}^{\text{cls}} F'_{b,q,h,w} + b_c^{\text{cls}}, \quad 1 \leq c \leq C. \quad (10)$$

Class posteriors are obtained by a temperature-scaled softmax over the class dimension with $\tau = 1$ during training and inference,

$$P_{b,c,h,w} = \frac{\exp(Z_{b,c,h,w}/\tau)}{\sum_{c'=1}^C \exp(Z_{b,c',h,w}/\tau)}, P \in \mathbb{R}^{B \times C \times 256 \times 256}. \quad (11)$$

Training minimizes a class-balanced cross-entropy on the fused logits with an ignore mask for unlabeled pixels. Let Ω be the set of labeled pixels over a mini-batch and $y_{b,c,h,w} \in \{0, 1\}$ the one-hot targets. Class weights w_c follow median-frequency balancing with pixel frequencies f_c measured on the training set, that is $w_c = \text{median}(f_1, \dots, f_C) / f_c$. The primary loss is

$$\mathcal{L}_{\text{ce}} = -\frac{1}{|\Omega|} \sum_{(b,h,w) \in \Omega} \sum_{c=1}^C w_c y_{b,c,h,w} \log P_{b,c,h,w}. \quad (12)$$

To improve robustness to class imbalance and to sharpen thin weed boundaries, we add a soft Dice term and an edge-aware term computed on the labeled pixels. Let $P_{b,c,h,w}$ be the fused posterior in (11) and $y_{b,c,h,w}$ the one-hot target. The Dice loss is

$$\mathcal{L}_{\text{dice}} = 1 - \frac{2 \sum_{(b,h,w) \in \Omega} \sum_{c=1}^C P_{b,c,h,w} y_{b,c,h,w} + \epsilon}{\sum_{(b,h,w) \in \Omega} \sum_{c=1}^C P_{b,c,h,w} + \sum_{(b,h,w) \in \Omega} \sum_{c=1}^C y_{b,c,h,w} + \epsilon}. \quad (13)$$

For edge supervision, we compute boundary maps by a fixed Sobel operator ∇ applied channel-wise to the class posteriors and labels. Define $E(P) = \sum_{c=1}^C \|\nabla P_c\|_1$ and $E(y) = \sum_{c=1}^C \|\nabla y_c\|_1$ on Ω . The edge loss uses an ℓ_1 penalty

$$\mathcal{L}_{\text{edge}} = \frac{1}{|\Omega|} \sum_{(b,h,w) \in \Omega} |E(P)_{b,h,w} - E(y)_{b,h,w}|. \quad (14)$$

The fused objective is the weighted combination

$$\mathcal{L}_{\text{fuse}} = \mathcal{L}_{\text{ce}} + \lambda_{\text{dice}} \mathcal{L}_{\text{dice}} + \lambda_{\text{edge}} \mathcal{L}_{\text{edge}}, \quad (15)$$

where λ_{dice} and λ_{edge} are fixed across all experiments.

The total objective is $\mathcal{L} = \mathcal{L}_{\text{fuse}} + \alpha \mathcal{L}_{\text{aux}}^{\text{idx}}$ with $\alpha = 0.3$, where $\mathcal{L}_{\text{aux}}^{\text{idx}}$ is the auxiliary cross-entropy applied to Y^{idx} after a 1×1 prediction layer. Gradients flow through the fusion block into both branches. At inference, the per-pixel label is $\hat{c}_{b,h,w} = \arg \max_c P_{b,c,h,w}$ and the corresponding confidence is $\max_c P_{b,c,h,w}$, which is exported with the segmentation map for downstream decision modules.

4. Results

We report results for the proposed radiance-index two-stream model on BAWSeg under three deployment-oriented protocols, namely within-plot, cross-plot, and cross-year. Performance is computed on held-out spatial blocks using mean Intersection over Union (mIoU), per-class IoU, micro-averaged precision, recall and F1, overall accuracy (OA), and Cohen's κ [49]. For mIoU confidence intervals (CI), we use a block bootstrap that resamples test blocks with replacement and recomputes the metric per replicate [50]. Unless stated otherwise, all metrics exclude ignore pixels.

4.1. Experimental Setting

Hardware and software. All experiments ran on a single workstation with Ubuntu 22.04.4 LTS, an AMD Ryzen 9 7950X CPU, 32 GB RAM, a 2 TB NVMe SSD, and one NVIDIA GeForce RTX 4090 GPU with 24 GB VRAM. The software stack used Python 3.10 and PyTorch 2.7 with CUDA 12.6. Training used automatic mixed precision, and evaluation used FP32. For reproducibility, we fixed a single global seed of 2026 across Python, NumPy, and PyTorch. We disabled cuDNN benchmarking and enabled deterministic algorithms where available, following PyTorch reproducibility guidance [51].

Training configuration. Models were trained for 50 epochs on 256×256 patches. Optimization used AdamW [52] with $\beta_1=0.9$, $\beta_2=0.999$, weight decay 0.01, and gradient clipping with a global norm of 1.0. The initial learning rate was set to 6×10^{-4} and decayed with a cosine schedule after a linear warm-up of 1500 iterations. The effective batch size was 16. Inputs were standardized per band or per index using training-set statistics. Data augmentation used spatial transforms only, including random horizontal and vertical flips and random rotations in $\{0^\circ, 90^\circ, 180^\circ, 270^\circ\}$, which preserves calibrated reflectance semantics.

Losses and inference. Training minimized a class-balanced cross-entropy on fused logits with an ignore mask, plus an auxiliary cross-entropy applied to the index stream with weight $\alpha=0.3$. Inference used single-scale evaluation at native patch resolution. For block-level evaluation, we

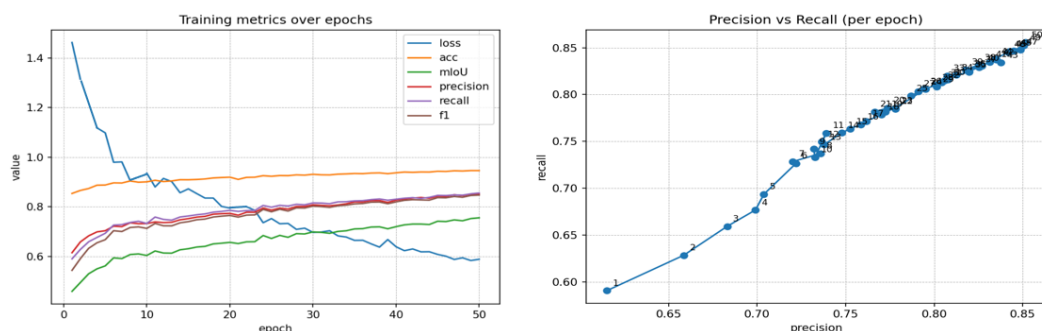


Figure 6. Training dynamics of the proposed model. The upper panel shows loss, accuracy, mean IoU, precision, recall and F1 over 50 epochs. The lower panel shows precision versus recall for each epoch. Markers move towards the upper right region as training progresses and stabilise near the final operating point.

Table 1. Within plot segmentation performance per year and field on held out test blocks. Mean IoU is estimated using 95% bootstrap confidence intervals. Precision, recall and F1 are micro averaged over all classes.

Year	Field	mIoU	Per class IoU			Micro metrics			Global metrics	
			Crop	Weed	Other	P	R	F1	OA	κ
2020	E2	0.748	0.842	0.621	0.781	0.838	0.846	0.842	0.943	0.784
	E8	0.751	0.844	0.623	0.786	0.840	0.848	0.844	0.944	0.786
2021	E2	0.754	0.845	0.626	0.791	0.842	0.850	0.846	0.945	0.789
	E8	0.759	0.848	0.630	0.800	0.844	0.852	0.848	0.946	0.791
2022	E2	0.762	0.850	0.636	0.801	0.846	0.854	0.850	0.947	0.795
	E8	0.760	0.849	0.633	0.798	0.845	0.853	0.849	0.947	0.793
2023	E2	0.757	0.846	0.632	0.794	0.843	0.851	0.847	0.946	0.792
	E8	0.763	0.851	0.638	0.800	0.848	0.856	0.852	0.948	0.799

applied a sliding-window over each held-out block using 256×256 windows with stride 128 and averaged logits in overlapping regions before taking the argmax label map. This prevents boundary artifacts from dominating block metrics.

Metrics and confidence intervals. For class c , IoU is $\text{IoU}_c = \frac{\text{TP}_c}{\text{TP}_c + \text{FP}_c + \text{FN}_c}$ computed over labeled pixels. Mean IoU averages over the three classes. Micro-precision, micro-recall, and micro-F1 are computed from the summed confusion counts across all classes and all blocks. Cohen’s κ is computed from the confusion matrix using standard chance correction for nominal labels [49]. For each reported CI, we draw 10,000 bootstrap replicates at the block level and take the 2.5 and 97.5 percentiles of the resulting mIoU distribution [50]. Block-level resampling is used because adjacent pixels inside an orthomosaic are spatially correlated, and evaluation based on spatially independent partitions is the standard practice in remote sensing segmentation benchmarks [53].

4.2. Segmentation Across Plots and Years

Figure 6 summarizes training dynamics across 50 epochs. The fused loss decreases steadily and validation mIoU increases until convergence, with the best checkpoint selected by validation mIoU. The final checkpoint is used for all protocol evaluations.

Table 1 reports within-plot performance stratified by year and field. Mean IoU remains in the range [0.748, 0.763] across the eight year-field combinations, with weed IoU consistently above 0.62. Micro-F1 remains close to 0.84, while OA remains close to 0.95 and κ remains close to 0.79. These results indicate stable behavior across acquisition years for the same operational region and sensor configuration.

Table 2 summarizes protocol-level generalization. Under within-plot evaluation, the model reaches mIoU 0.756 ± 0.004 with weed IoU 0.635. Under cross-plot transfer, training on one field and testing on the other yields mIoU near 0.71, and the primary degradation appears in the weed

Table 2. Segmentation performance under different evaluation protocols. Train and test sets are defined at the block level. Mean IoU is reported with 95% confidence intervals.

Protocol	Train set	Test set	mIoU \pm CI	Per class IoU			Micro metrics			Global metrics	
				Crop	Weed	Other	P	R	F1	OA	κ
Within plot	E2 and E8, 2020 to 2023	E2 and E8, 2020 to 2023	0.756 \pm 0.004	0.847	0.635	0.794	0.851	0.843	0.847	0.946	0.794
Cross plot	E2, 2020 to 2023	E8, 2020 to 2023	0.712 \pm 0.006	0.840	0.576	0.724	0.838	0.830	0.834	0.937	0.768
Cross plot	E8, 2020 to 2023	E2, 2020 to 2023	0.718 \pm 0.006	0.846	0.584	0.724	0.842	0.836	0.839	0.939	0.773
Cross year	2020 to 2022, E2 and E8	2023, E2 and E8	0.692 \pm 0.007	0.832	0.544	0.700	0.828	0.816	0.822	0.936	0.752

Table 3. Comparison with classical baselines and modern segmentation networks under the within plot protocol on E2 and E8 from 2020 to 2023. MSI denotes the five calibrated multispectral bands and indices denote the five vegetation indices. Mean IoU is reported with 95% bootstrap confidence intervals over test blocks.

Method	Year / Venue	Input	mIoU \pm CI	Crop IoU	Weed IoU	Others IoU	F1	OA	κ	Params (M)
RF + Indices [54]	2021 ML	Indices	0.674 \pm 0.010	0.812	0.532	0.679	0.734	0.907	0.703	0.2
SegNet RGB [19]	2019 TPAMI	RGB	0.694 \pm 0.009	0.825	0.558	0.699	0.752	0.915	0.718	29.4
SegNet MSI [19]	2024 TPAMI	MSI	0.702 \pm 0.009	0.831	0.567	0.708	0.759	0.918	0.724	29.5
U-Net RGB [18]	2023 MICCAI	RGB	0.712 \pm 0.008	0.836	0.579	0.720	0.768	0.922	0.732	31.0
U-Net MSI [18]	2022 MICCAI	MSI	0.731 \pm 0.007	0.842	0.594	0.758	0.783	0.930	0.748	31.1
UNet++ MSI [55]	2024 DLMIA	MSI	0.735 \pm 0.007	0.844	0.603	0.759	0.787	0.932	0.751	34.2
DeepLabv3 R50 RGB [56]	2020 arXiv	RGB	0.724 \pm 0.008	0.838	0.585	0.748	0.775	0.928	0.743	41.1
DeepLabv3+ R50 MSI [20]	2024 ECCV	MSI	0.738 \pm 0.007	0.845	0.609	0.761	0.788	0.933	0.753	43.3
PSPNet R50 RGB [57]	2023 CVPR	RGB	0.720 \pm 0.008	0.835	0.582	0.743	0.772	0.927	0.739	46.3
HRNetV2 W18 MSI [58]	2022 TPAMI	MSI	0.740 \pm 0.007	0.846	0.611	0.763	0.792	0.934	0.756	65.8
BiSeNetV2 RGB [59]	2021 IJCV	RGB	0.707 \pm 0.009	0.829	0.566	0.726	0.764	0.921	0.729	13.4
SegFormer B0 RGB [40]	2021 NeurIPS	RGB	0.732 \pm 0.007	0.843	0.598	0.755	0.784	0.931	0.749	13.7
SegFormer B1 RGB [40]	2021 NeurIPS	RGB	0.736 \pm 0.007	0.846	0.602	0.760	0.787	0.933	0.752	27.6
SegFormer B1 MSI [40]	2023 NeurIPS	MSI	0.744 \pm 0.005	0.847	0.616	0.769	0.793	0.943	0.786	27.8
Ours	2026	MSI	0.756 \pm 0.004	0.847	0.635	0.794	0.847	0.946	0.794	22.8

class, while crop IoU remains close to the within-plot level. Under cross-year testing, training on 2020–2022 and testing on 2023 yields mIoU 0.692 \pm 0.007 and weed IoU 0.544, with crop IoU remaining above 0.83. Across protocols, the relative sensitivity is concentrated in weed IoU, while OA stays above 0.93, reflecting the strong class imbalance between vegetation and the less frequent weed pixels.

4.3. Comparison with Existing Methods

Table 3 compares the proposed model with an index-based classical baseline and representative CNN and Transformer segmentation networks under the within-plot protocol. All deep baselines were trained and evaluated using the same block splits, patch size, optimizer type, learning-rate schedule family, and number of epochs as the proposed model. For multispectral inputs, we adapted the first layer of each architecture to accept five channels. For models that use patch embeddings, we replaced the input projection to accept five channels and initialized added channel weights by copying the mean of RGB weights when ImageNet pretraining was used, then fine-tuned end-to-end on BAWSeg.

The random forest baseline uses the five vegetation indices as input features and predicts per-pixel labels, followed by a 3×3 majority filter to remove isolated predictions. It achieves mIoU 0.674 \pm 0.010 with weed IoU 0.532, which quantifies the gap between index-threshold style pipelines and learned dense segmentation on calibrated mosaics.

Among deep baselines, the strongest multispectral model in this comparison is SegFormer-B1 with MSI input, which achieves mIoU 0.744 \pm 0.005 and weed IoU 0.616. Convolutional multispectral models such as U-Net MSI and DeepLabv3+ MSI achieve mIoU in the 0.73 to 0.74 range with weed IoU below 0.61. The proposed two-stream fusion achieves mIoU 0.756 \pm 0.004 and weed IoU 0.635 with 22.8M parameters. Relative to SegFormer-B1 MSI, this corresponds to a +0.012 absolute improvement in mIoU and a +0.019 improvement in weed IoU under matched splits and evaluation. These gains are consistent with separating calibrated radiance cues from index cues

Table 4. Ablation on the within-plot protocol. Δ is relative to the full model. Params in millions. FLOPs in billions at 256×256 . Mem in GB at FP16, batch size 1. mIoU reports block-bootstrap 95% confidence intervals.

Variant	mIoU \uparrow	Δ	Weed IoU \uparrow	Params(M) \downarrow	FLOPs(G) \downarrow	Mem(GB) \downarrow	FPS \uparrow
<i>Module removal or replacement</i>							
Full model	0.756 \pm 0.004	0.000	0.635	22.8	33.6	2.60	78
w/o VIMB (RAW only)	0.731 \pm 0.007	-0.025	0.596	9.6	25.4	2.20	92
w/o relative bias in WSA	0.749 \pm 0.007	-0.007	0.626	12.8	33.4	2.60	78
w/o Slot Attention	0.744 \pm 0.007	-0.012	0.618	12.3	32.4	2.50	80
w/o mean-slot broadcast	0.748 \pm 0.007	-0.008	0.622	12.3	32.4	2.50	80
Single-scale decoder (idx stream)	0.747 \pm 0.007	-0.009	0.621	12.6	32.7	2.55	80
<i>Quantity changes</i>							
WSA heads $h=4$	0.750 \pm 0.007	-0.006	0.627	12.8	33.5	2.60	78
WSA heads $h=8$ (full)	0.756 \pm 0.004	0.000	0.635	12.8	33.6	2.60	78
WSA heads $h=12$	0.758 \pm 0.007	+0.002	0.637	12.9	34.4	2.70	74
Mamba layers $L=0$	0.738 \pm 0.007	-0.018	0.610	12.2	31.5	2.50	82
Mamba layers $L=1$	0.746 \pm 0.007	-0.010	0.624	12.5	32.5	2.55	79
Mamba layers $L=2$ (full)	0.756 \pm 0.004	0.000	0.635	12.8	33.6	2.60	78
Mamba layers $L=3$	0.757 \pm 0.007	+0.001	0.637	13.1	34.9	2.70	75

Notes. FLOPs: measured with `fvcore` (count MACs as FLOPs), input $1 \times C \times 256 \times 256$, `eval()` and Dropout off. Mem: PyTorch max-allocated GPU memory (FP16, batch= 1). FPS: average over 200 iterations after 20 warm-up, timing wrapped by `torch.cuda.synchronize()`. Unless noted, differences ≤ 0.007 mIoU are not statistically significant under block-level bootstrap.

and fusing them at native resolution, rather than forcing a single encoder to learn both signal types from a concatenated input.

4.4. Ablation Study

Table 4 reports ablations under the within-plot protocol. Each variant modifies one factor while keeping the same training configuration, random seed, optimizer, schedule, and data splits. Reported mIoU values include block-bootstrap CIs computed with the same procedure as the main results. Throughput is measured at batch size 1 using FP16 inference on an RTX 4090, with 20 warm-up iterations and 200 timed iterations, and GPU timing synchronized before and after each iteration.

Removing the vegetation-index modeling branch yields the largest accuracy drop, reducing mIoU from 0.756 to 0.731 and weed IoU from 0.635 to 0.596, while reducing parameters and increasing FPS. This isolates the contribution of index-based context beyond what is learned from calibrated multispectral bands alone. Within the index stream, removing relative positional bias in windowed self-attention reduces mIoU to 0.749, and removing Slot Attention reduces mIoU to 0.744 with a concurrent weed IoU decrease, indicating that grouping tokens into region descriptors contributes to weed discrimination under canopy mixing. Removing the mean-slot broadcast reduces mIoU to 0.748, which shows that re-injecting a global descriptor into the spatial grid affects final predictions beyond the slot aggregation itself.

Varying attention heads shows a compute-accuracy trade-off. Reducing heads to $h=4$ decreases mIoU to 0.750 with a minor weed IoU decrease. Increasing heads to $h=12$ yields mIoU 0.758 while reducing FPS due to higher attention cost. For the state-space component, removing Mamba layers produces a clear reduction to 0.738 mIoU and 0.610 weed IoU, and performance improves monotonically up to two layers, with limited change from two to three layers at increased compute and memory. Across these variants, improvements below the ablation CI scale in Table 4 should be interpreted as small under the block-bootstrap uncertainty, while changes above that scale correspond to consistent differences under the same evaluation procedure.

5. Discussion

The evaluation protocols expose two distinct regimes. When training and testing on disjoint spatial blocks from the same paddocks and seasons, VISA reaches 0.756 mIoU and 0.635 weed IoU, indicating that the model can separate weed patches from barley canopy at orthomosaic

resolution while preserving row structure. Under cross-plot testing, mIoU drops to about 0.71 and the degradation concentrates on the weed class, while crop IoU remains close to the within-plot level. The same pattern holds under cross-year testing, where mIoU decreases to 0.692 and weed IoU to 0.544 with crop IoU still above 0.83. This behaviour is consistent with operational conditions in cereal systems, where crop appearance is relatively regular within a growth stage, while weed pressure, phenology, and within-row occlusion vary strongly across paddocks and seasons. The results therefore suggest that the remaining generalization gap is driven less by background and crop variation and more by shifts in weed morphology, density, and canopy mixing.

A key design choice in VISA is to prevent the radiance cues and index cues from competing inside a single encoder. Vegetation indices suppress many illumination and exposure effects by construction and encode cross-band interactions that correlate with chlorophyll and canopy vigor, which makes them informative for vegetation delineation across flights. At the same time, indices compress radiometric detail and can attenuate subtle within-canopy contrasts that differentiate sparse weeds from barley leaves, especially when the canopy is dense and when soil is largely occluded. Conversely, calibrated multispectral reflectance retains high-frequency textures, row boundaries, and small spectral deviations that are informative for fine weed clusters, but this signal is more sensitive to residual radiometric drift and to local mosaic artefacts. VISA keeps these cues in separate pathways so that the radiance stream can preserve boundary detail without being dominated by normalized ratios, and the index stream can capture stable vegetation patterns without being distracted by band-specific noise. The fusion at native resolution then combines boundary precision from the radiance stream with context from the index stream, which aligns with the observed gains over a single-stream SegFormer baseline at similar scale.

The ablation study helps interpret which components contribute to weed robustness. Removing the index branch reduces mIoU by 0.025 and lowers weed IoU from 0.635 to 0.596, indicating that vegetation-index reasoning contributes materially beyond what can be learned from calibrated bands alone. Within the index branch, windowed self-attention supports local structure and row-consistent patterns, and the relative positional bias yields a consistent mIoU reduction when removed, which is expected because row geometry is expressed primarily through relative offsets rather than absolute location in a tile. The state-space layers provide the largest single improvement among the index-branch modules, with a 0.018 mIoU drop when they are removed, which suggests that linear-time context propagation helps encode plot-scale regularities that extend beyond the attention window. Slot Attention further improves weed sensitivity, with a 0.012 mIoU drop when removed, consistent with the role of region-level grouping in stabilizing representations of sparse and fragmented weed patches embedded in crop canopy. The mean-slot broadcast contributes an additional margin, indicating that injecting a global descriptor back to the spatial grid helps resolve local ambiguity in mixed pixels.

BAWSeg is constructed to make these conclusions meaningful under realistic deployment constraints. The dataset spans four seasons across two commercial paddocks, includes calibrated five-band orthomosaics and a consistent set of vegetation indices, and uses leakage-free spatial blocks for training and testing. Block splits are critical in orthomosaic learning because random sampling can place near-duplicate textures and lighting conditions in both training and test sets, yielding optimistic estimates that do not translate across paddocks. The cross-plot and cross-year protocols further stress the model under changes in weed distribution and season-specific appearance, which are the primary sources of failure in practice. The relatively stable crop IoU across protocols indicates that the calibration and preprocessing pipeline produces consistent crop appearance, while the weed IoU drop under shift highlights the need for modelling choices and training strategies that target rare, small, and occluded weed structures.

From a precision agriculture perspective, the reported performance is most relevant when translated into actionable maps. The model outputs per-pixel posteriors that can be aggregated into patch-level weed objects and converted into prescription maps using minimum-area constraints

that match sprayer resolution and drift tolerance. In this setting, false positives are often more costly than small boundary errors, because over-spraying increases chemical use and can accelerate resistance. The confidence maps produced by the softmax output enable risk-aware filtering, where low-confidence weed detections can be flagged for targeted scouting rather than immediate treatment. The inference throughput reported in the ablation table indicates that the architecture is compatible with practical offline processing of field-scale orthomosaics on a single GPU, which matches common agronomic workflows that generate maps after flight rather than on the UAV.

Several limitations remain. First, the geographic scope is limited to two paddocks in one grainbelt region and one UAV sensor configuration, so the reported cross-year robustness does not fully characterize transfer to different soil types, management practices, or imaging systems. Second, the labels represent three classes and resolve crop and weed overlap by polygon precedence, which is operationally convenient but does not capture the fractional composition of mixed pixels in dense canopy. This affects both training targets and evaluation, especially when weeds are small and partially occluded. Third, orthomosaic generation can introduce seamline artefacts and local blur that change with overlap and wind conditions, which can act as nuisance variation across campaigns. Addressing these constraints motivates several concrete directions. Expanding BAWSeg to additional farms and sensors would improve coverage of radiometric and agronomic variability. Introducing probabilistic or soft labels near ambiguous boundaries and in mixed canopy regions would better match the underlying physical mixture. For generalization, domain generalization and test-time adaptation strategies that operate on calibrated reflectance and indices are promising, since the cross-plot and cross-year drops are concentrated in the weed class. Finally, weakly supervised extensions that exploit unlabeled mosaics from new seasons could reduce annotation burden while improving robustness to the shifts that are most salient in deployment.

6. Conclusions

In this paper, we presented BAWSeg, a four-year UAV multispectral benchmark for barley weed segmentation collected over two commercial paddocks in Western Australia. BAWSeg provides radiometrically calibrated five-band reflectance orthomosaics (blue, green, red, red edge, and near-infrared), derived vegetation-index maps, and dense pixel annotations for crop, weed, and other classes, together with leakage-free spatial block splits and deployment-oriented evaluation protocols. Building on this benchmark, we proposed VISA, a two-stream segmentation architecture that decouples radiance-based learning from vegetation-index reasoning and fuses both cues at native resolution to improve robustness under mixed canopy conditions. Across the BAWSeg evaluation suite, VISA achieves a within-plot mIoU of 0.756 with weed IoU of 0.635 and overall accuracy of 0.946 using 22.8M parameters, and it retains mIoU of 0.712 under cross-plot transfer and 0.692 under cross-year testing.

Beyond accuracy gains, our results show that explicitly modeling vegetation-index structure complements calibrated radiance features and improves weed sensitivity under challenging field variability. The ablation study supports this conclusion: removing the index branch yields a 0.025 mIoU decrease, indicating that index-driven context contributes materially to final predictions. BAWSeg and VISA together offer a reproducible foundation for benchmarking multispectral crop-weed segmentation under realistic spatial and temporal shifts, and for developing models that better generalize across seasons and paddocks. To facilitate follow-up research and practical adoption, we will release the BAWSeg dataset, the VISA implementation, and trained model weights upon publication.

Author Contributions: Conceptualization, H.W. and A.M.; Methodology, H.W., M.I. and A.M.; Software, H.W.; Validation, H.W., M.I., D.S. and X.W.; Formal analysis, H.W.; Investigation, H.W., M.I. and D.S.; Resources, M.I., D.S. and A.M.; Data curation, H.W., M.I., D.S. and X.W.; Writing—original draft preparation, H.W.; Writing—review and editing, H.W., M.I., D.S., X.W. and A.M.; Visualization, H.W. and X.W.; Supervi-

sion, A.M.; Project administration, A.M. and M.I.; Funding acquisition, A.M. and M.I. All authors have read and agreed to the published version of the manuscript.

Funding: Not applicable.

Institutional Review Board Statement: Not applicable.

Informed Consent Statement: Not applicable.

Data Availability Statement: The BAWSeg dataset, the VISA implementation, and trained model weights will be made publicly available upon publication of this article. The public repository links and persistent identifiers (DOI), as well as detailed usage documentation, will be provided in the final published version.

Acknowledgments: The authors acknowledge the support from The University of Western Australia and the Department of Primary Industries and Regional Development (DPIRD), Government of Western Australia. We thank the field site owners and operational staff in the Kondinin region for enabling repeated UAV data collection across multiple seasons, and we acknowledge the assistance and advice from collaborators involved in field logistics, data curation, and annotation quality control. The authors reviewed and edited the content and take full responsibility for the final manuscript.

Conflicts of Interest: The authors declare no conflicts of interest. The funders had no role in the design of the study; in the collection, analyses, or interpretation of data; in the writing of the manuscript; or in the decision to publish the results.

Abbreviations

The following abbreviations are used in this manuscript:

BAWSeg	Barley Weed Segmentation benchmark dataset
VISA	Vegetation-Index and Spectral Attention (two-stream segmentation network)
UAV	Unmanned Aerial Vehicle
RPAS	Remotely Piloted Aircraft System
RTK	Real-Time Kinematic
RGB	Red, Green, and Blue
NIR	Near-Infrared
RE	Red Edge
NDVI	Normalized Difference Vegetation Index
GNDVI	Green Normalized Difference Vegetation Index
EVI	Enhanced Vegetation Index
SAVI	Soil-Adjusted Vegetation Index
MSAVI	Modified Soil-Adjusted Vegetation Index
SIFT	Scale-Invariant Feature Transform
RANSAC	Random Sample Consensus
WSA	Windowed Self-Attention
SE	Squeeze-and-Excitation
CBAM	Convolutional Block Attention Module
GRU	Gated Recurrent Unit
mIoU	mean Intersection over Union
IoU	Intersection over Union
OA	Overall Accuracy
CI	Confidence Interval
FP16	16-bit Floating Point
FP32	32-bit Floating Point

References

1. ABARES. Australian Crop Report. Technical Report Issue 2023, Australian Bureau of Agricultural and Resource Economics and Sciences (ABARES), Canberra, Australia, 2023. Accessed: 2025-11-13.

2. Grain Industry Association of Western Australia. Barley Council Crop Report and Industry Outlook. Technical report, 2023. Grain Industry Association of Western Australia, Perth.
3. Pacanoski, Z.; Mehmeti, A. Weeds and Their Impact on Crop Production. *Plants* **2021**, *10*, 1–18.
4. Oerke, E.C.; Dehne, H.W.; Schönbeck, F. Yield Losses in Major Crops Due to Weeds and Other Pests. *Crop Protection* **2021**, *143*, 105552.
5. Llewellyn, R.; Ronning, D.; Ouzman, J.; Walker, S.; Mayfield, A.; Clarke, M. Impact of Weeds on Australian Grain Production. Technical report, Grains Research and Development Corporation (GRDC), Canberra, Australia, 2016.
6. Powles, S.B.; Yu, Q. Evolution in Action: Plants Resistant to Herbicides. *Annual Review of Plant Biology* **2010**, *61*, 317–347.
7. Walsh, M.J.; Harrington, R.B.; Powles, S.B. Harrington Seed Destructor: A New Non Chemical Weed Control Tool for Global Grain Crops. *Crop Science* **2012**, *52*, 1343–1347.
8. Broster, J.C.; Koetz, E.; Wu, H. A Survey of Weed Flora and Weed Management Practices in the Australian Grain Industry. *Weed Biology and Management* **2019**, *19*, 111–120.
9. Reeves, T.G.; Code, G.; Sutherland, A. The Effect of Annual Ryegrass (*Lolium rigidum*) on Yield of Cereals in Mediterranean Type Environments. *Australian Journal of Experimental Agriculture* **2018**, *58*, 412–420.
10. Hashem, A.; Borger, C.; Pathan, S.; et al. Wild Radish (*Raphanus raphanistrum*) Interference in Barley and Wheat in Western Australia. *Crop and Pasture Science* **2020**, *71*, 705–715.
11. Chlingaryan, A.; Sukkariéh, S.; Whelan, B. Machine Learning Approaches for Crop Yield Prediction and Nitrogen Status Estimation in Precision Agriculture: A Review. *Computers and Electronics in Agriculture* **2018**, *151*, 61–69.
12. Lambert, J.; Tisseyre, B.; Guillaume, S. Weed Mapping in Arable Fields Using Low Altitude Imagery Acquired by Unmanned Aerial Vehicles. *Precision Agriculture* **2018**, *19*, 684–698.
13. López-Granados, F. Weed Detection for Site Specific Weed Management: Mapping and Real Time Approaches. *Weed Research* **2011**, *51*, 1–11.
14. López-Granados, F.; Torres-Sánchez, J.; De Castro, A.I.; Serrano-Pérez, A.; Mesas-Carrascosa, F.J.; Peña, J.M. Early Season Weed Mapping in Sunflower Using UAV Technology: Variability of Herbicide Treatment Maps Against Weed Thresholds. *Precision Agriculture* **2016**, *17*, 183–199.
15. Pérez-Ortiz, M.; Peña, J.M.; Gutiérrez, P.A.; Torres-Sánchez, J.; Hervas-Martínez, C.; López-Granados, F. Selecting Patterns and Features for Between and Within Crop Row Weed Mapping Using UAV Imagery. *Expert Systems with Applications* **2016**, *47*, 85–94.
16. Jin, X.; Xu, X.; Yang, G.; Feng, H.; Li, Z.; Shen, J. Consistent Improvements in Weed Mapping Performance in Corn Fields Leveraging Multisource Remote Sensing Data and Machine Learning Methods. *Frontiers in Plant Science* **2023**, *14*, 1237256.
17. Li, H.; Wang, Z.; Zhang, Y.; et al. A Systematic Review of Deep Learning for Weed Detection. *Artificial Intelligence in Agriculture* **2023**, *7*, 1–17.
18. Ronneberger, O.; Fischer, P.; Brox, T. U Net: Convolutional Networks for Biomedical Image Segmentation. In Proceedings of the Medical Image Computing and Computer Assisted Intervention, 2015, pp. 234–241.
19. Badrinarayanan, V.; Kendall, A.; Cipolla, R. SegNet: A Deep Convolutional Encoder Decoder Architecture for Image Segmentation. *IEEE Transactions on Pattern Analysis and Machine Intelligence* **2017**, *39*, 2481–2495.
20. Chen, L.C.; Zhu, Y.; Papandreou, G.; Schroff, F.; Adam, H. Encoder Decoder with Atrous Separable Convolution for Semantic Image Segmentation. In Proceedings of the European Conference on Computer Vision, 2018, pp. 801–818.
21. Lottes, P.; Behley, J.; Milioto, A.; Stachniss, C. UAV-based Crop and Weed Classification Using Fully Convolutional Networks. In Proceedings of the ICRA, 2017, pp. 5157–5163.
22. Wang, H.; Ibrahim, M.; Miao, Y.; Severtson, D.; Mansoor, A.; Mian, A.S. Multispectral Remote Sensing for Weed Detection in West Australian Agricultural Lands. In Proceedings of the 2024 International Conference on Digital Image Computing: Techniques and Applications (DICTA). IEEE, 2024, pp. 624–631.
23. Peña, J.M.; Torres-Sánchez, J.; de Castro, A.I.; Kelly, M.; López-Granados, F. Weed Mapping in Early Season Maize Fields Using Object Based Analysis of Unmanned Aerial Vehicle Images. *PLoS ONE* **2013**, *8*, e77151.
24. Wang, H.; Wang, Y.; Wang, X.; Miao, Y.; Zhang, Y.; Zhang, Y.; Mansoor, A. P2MFDS: A Privacy-Preserving Multimodal Fall Detection System for Elderly People in Bathroom Environments. In Proceedings of the International Conference on Artificial Intelligence of Things and Systems. Springer, 2025, pp. 129–146.
25. De Castro, A.I.; Torres-Sánchez, J.; Peña, J.M.; Jiménez-Brenes, F.M.; Csillik, O.; López-Granados, F. An Automatic Random Forest OBIA Algorithm for Early Weed Mapping Between and Within Crop Rows Using UAV Imagery. *Remote Sensing* **2018**, *10*, 285.
26. Castaldi, F.; Pelosi, F.; Pascucci, S.; Casa, R. Assessing the Potential of Images from Unmanned Aerial Vehicles to Support Herbicide Patch Spraying in Maize. *Precision Agriculture* **2017**, *18*, 76–94.
27. Pérez-Ortiz, M.; Peña, J.M.; Gutiérrez, P.A.; Torres-Sánchez, J.; Hervas-Martínez, C.; López-Granados, F. A Semi Supervised System for Weed Mapping in Sunflower Crops Using Unmanned Aerial Vehicle Imagery. *Applied Soft Computing* **2015**, *37*, 533–544.
28. Ciceklidag, P.; et al. High-Definition 3D Point Cloud Mapping of the City of Subiaco in Western Australia. In Proceedings of the DICTA. IEEE, 2024.

29. Tamouridou, A.A.; Alexandridis, T.K.; Pantazi, X.E.; Lagopodi, A.L.; Kasampalis, D.A.; Moshou, D. Application of Multilayer Perceptron with Automatic Relevance Determination on Weed Mapping Using UAV Multispectral Imagery. *Sensors* **2017**, *17*, 2307.
30. Moshou, D.; Pantazi, X.E.; Alexandridis, T.; Bravo, C.; Whetton, R.; Mouazen, A.M. Towards Real Time Weed Detection Using Novelty Detection and UAV Multispectral Imaging. *Sensors* **2017**, *17*, 2007.
31. Ibrahim, M.; Akhtar, N.; Wang, H.; Anwar, S.; Mian, A. Multistream Network for LiDAR and Camera-based 3D Object Detection in Outdoor Scenes. In Proceedings of the 2025 IEEE/RSJ International Conference on Intelligent Robots and Systems (IROS). IEEE, 2025, pp. 7796–7803.
32. Ibrahim, M.; Wang, H.; A. Iqbal, I.; Miao, Y.; Albaqami, H.; Blom, H.; Mian, A. Forest stem extraction and modeling (FoSEM): a LiDAR-based framework for accurate tree stem extraction and modeling in radiata pine plantations. *Remote Sensing* **2025**, *17*, 445.
33. Fawakherji, M.; Kocamaz, D.; Sosa, D.; et al. Automated Weed Mapping in Cotton Using UAV Imagery and Deep Learning. *Remote Sensing* **2023**, *15*, 2287.
34. Shahi, T.; Howard, C.; McCool, C. Deep Learning Methods for Weed Mapping in Cropping Systems: A Comparative Study. *Drones* **2023**, *7*, 439.
35. Sa, I.; Chen, Z.; Popović, M.; McCool, R.I.; Dayoub, F.; Corke, P.; Upcroft, B. WeedMap: A Large-Scale Semantic Weed Mapping Framework Using Aerial Multispectral Imaging and Deep Neural Networks. *arXiv preprint arXiv:1809.08938* **2018**.
36. Gupta, A.; Kumar, R.; Sharma, P. Drone-Based Imagery and Deep Learning in Precision Agriculture: A Review. *Remote Sensing* **2023**, *15*, 4943.
37. Olsen, A.; Konovalov, D.A.; Ridd, P.; et al. DeepWeeds: A Multiclass Weed Species Image Dataset for Deep Learning. *Scientific Reports* **2019**, *9*, 1–12.
38. Dosovitskiy, A.; Beyer, L.; Kolesnikov, A.; Weissenborn, D.; Zhai, X.; Unterthiner, T.; Dehghani, M.; Minderer, M.; Heigold, G.; Gelly, S.; et al. An Image is Worth 16x16 Words: Transformers for Image Recognition at Scale. In Proceedings of the International Conference on Learning Representations, 2021.
39. Liu, Z.; Lin, Y.; Cao, Y.; Hu, H.; Wei, Y.; Zhang, Z.; Lin, S.; Guo, B. Swin Transformer: Hierarchical Vision Transformer Using Shifted Windows. In Proceedings of the Proceedings of the IEEE/CVF International Conference on Computer Vision (ICCV), 2021, pp. 10012–10022.
40. Xie, E.; Wang, W.; Yu, Z.; Anandkumar, A.; Alvarez, J.M.; Luo, P. SegFormer: Simple and Efficient Design for Semantic Segmentation with Transformers. In Proceedings of the Advances in Neural Information Processing Systems, 2021.
41. Zuo, X.; Huang, X.; Wang, Y.; Li, J. MSViT: Multi-Scale Vision Transformer for Remote Sensing Image Segmentation. *Remote Sensing* **2022**, *14*, 5563.
42. Li, Q.; Peng, J.; Zhang, L.; Wang, Y. RSTFormer: Remote Sensing Transformer for Semantic Segmentation of High-Resolution Aerial Images. *IEEE Transactions on Geoscience and Remote Sensing* **2022**.
43. Li, Z.; Chen, H.; He, X.; Li, Y.; Cheng, G.; Li, X. UNetFormer: A UNet-like Transformer for Efficient Semantic Segmentation of Remote Sensing Images. *IEEE Transactions on Geoscience and Remote Sensing* **2023**, *61*, 1–15.
44. Kong, L.; Ma, L.; Fang, L.; Liu, X. SpectralFormer: Rethinking Hyperspectral Image Classification with Transformers. *IEEE Transactions on Geoscience and Remote Sensing* **2022**, *60*, 1–15.
45. Sandoval-Pillajo, D.; Torres, D.; Valarezo, E.; García, G. A Vision Transformer Approach for Automatic Weed Detection in Maize Fields. *Electronics* **2025**, *14*, 421.
46. Uysal, G.; Ozdemir, S.; Cetin, B. WeedSense: A Hybrid CNN–Transformer Network for Real-Time Weed Segmentation from UAV Imagery. *Computers and Electronics in Agriculture* **2024**, *218*, 108628.
47. Guo, H.; Xie, E.; Zhang, C.; Li, Z.; Luo, P. VMamba: Visual State Space Model. *arXiv preprint arXiv:2310.11458* **2023**.
48. Ma, Y.; Ji, Y.; Cao, J.; Zhang, W. RS3Mamba: Visual State Space Model for Remote Sensing Image Semantic Segmentation. *arXiv preprint arXiv:2404.02457* **2024**.
49. Cohen, J. A Coefficient of Agreement for Nominal Scales. *Educational and Psychological Measurement* **1960**, *20*, 37–46. <https://doi.org/10.1177/001316446002000104>.
50. Efron, B.; Tibshirani, R.J. *An Introduction to the Bootstrap*; Chapman & Hall/CRC Monographs on Statistics and Applied Probability, Chapman and Hall/CRC: New York, NY, USA, 1994.
51. PyTorch Contributors. Reproducibility. PyTorch Documentation, 2025. Accessed: 2026-02-16.
52. Loshchilov, I.; Hutter, F. Decoupled Weight Decay Regularization. In Proceedings of the International Conference on Learning Representations, 2019. arXiv:1711.05101.
53. Wang, J.; Yang, W.; Zhang, X.; Huang, G.; Qian, J. LoveDA: A Remote Sensing Land-Cover Dataset for Domain Adaptive Semantic Segmentation. *arXiv preprint arXiv:2110.08733* **2021**.
54. Breiman, L. Random Forests. *Machine Learning* **2001**, *45*, 5–32.
55. Zhou, Z.; Siddiquee, M.M.R.; Tajbakhsh, N.; Liang, J. UNet++: A Nested U Net Architecture for Medical Image Segmentation. In Proceedings of the Deep Learning in Medical Image Analysis and Multimodal Learning for Clinical Decision Support, 2018, pp. 3–11.
56. Chen, L.C.; Papandreou, G.; Schroff, F.; Adam, H. Rethinking Atrous Convolution for Semantic Image Segmentation. *arXiv preprint arXiv:1706.05587* **2017**.

57. Zhao, H.; Shi, J.; Qi, X.; Wang, X.; Jia, J. Pyramid Scene Parsing Network. In Proceedings of the IEEE Conference on Computer Vision and Pattern Recognition, 2017, pp. 2881–2890.
58. Wang, J.; Sun, K.; Cheng, T.; Jiang, B.; Deng, C.; Zhao, Y.; Liu, D.; Mu, Y.; Tan, M.; Wang, X.; et al. Deep High Resolution Representation Learning for Visual Recognition. *IEEE Transactions on Pattern Analysis and Machine Intelligence* **2020**, *43*, 3349–3364.
59. Yu, C.; Gao, J.; Wang, C.; Yu, G.; Shen, C.; Sang, N. BiSeNet V2: Bilateral Network with Guided Aggregation for Real Time Semantic Segmentation. *International Journal of Computer Vision* **2021**, *129*, 3051–3072.

Disclaimer/Publisher’s Note: The statements, opinions and data contained in all publications are solely those of the individual author(s) and contributor(s) and not of MDPI and/or the editor(s). MDPI and/or the editor(s) disclaim responsibility for any injury to people or property resulting from any ideas, methods, instructions or products referred to in the content.